Short-range structural correlations in amorphous 2D polymers

Patrick Alexa,[a] Christina Oligschleger,[b] Pascal Gröger,[a] Claudius Morchutt,[a,c] Vijay Vyas,[a] Bettina V. Lotsch,[a,d] J. Christian Schön,[a] Rico Gutzler,*[a] and Klaus Kern[a,c]

Abstract: Many 2D covalent polymers synthesized as single layers on surfaces show inherent disorder, expressed for example in their ring-size distribution. Systems which are expected to form the thermodynamically favored hexagonal lattice usually deviate from crystallinity and include high numbers of pentagons, heptagons, and rings of other sizes. Here we investigate the amorphous structure of two different covalent polymers in real space using scanning tunneling microscopy. Molecular dynamics simulations are employed to extract additional information. We show that short-range correlations exist in the structure of one polymer, i.e. that polygons are not tessellating the surface randomly but that ring neighborhoods have preferential compositions. The correlation is dictated by the energy of formation of the ring neighborhoods.

Introduction

Recent years have witnessed a surge of synthesis methods for 2D polymers, in which molecular repeat units are not connected in 1D strings like in common organic polymers, but rather in a plane due to more than two connection sites per repeat unit. Reversible chemistry yields the formation of comparably ordered 2D sheets in covalent organic frameworks (COFs),[1] in which existing defects can be healed out by post-synthetic modifications.[2] In the surface-science approach to 2D polymers the bond formation is often non-reversible.[3] Consequently, once a bond is formed – even if this leads to an energetically expensive defect – it cannot be easily opened anymore to heal out the defect in order for the polymer to evolve towards a thermodynamic minimum. Two-dimensional architectures built up from organic molecules are thus prone to include crystallographic defects if error-correction mechanisms are not available. Many 2D (metal-)organic networks exhibit some kind of disorder. Branched covalent 2D polymeric structures are reported[4] alongside random 2D metal-organic string networks[5]. Other 2D porous metal-organic networks grow into amorphous structures due to the entropic stabilization provided by conformational disorder.[6] Porous covalent polymers other than single-layer COFs were reported to be generally amorphous[7–10], and Monte Carlo simulations were applied to disentangle how precursor mobility and surface reactivity influence structure growth.[11,12] Independently, Monte Carlo simulations grant insight into the amorphous assembly of tripod-shaped molecular building blocks confined to a surface.[13] Defect densities in the form of pore-size distributions were extracted from experimental data and the effect of the polymerization temperature was investigated.[12] In spite of all these efforts to study growth conditions, finding design principles that allow the fabrication of well-ordered single layer covalent networks via C–C coupling remains mostly elusive. For the special case of boronic acid condensation reactions in the synthesis of single-layer COFs, the presence of excess water as a reaction regulator renders the reaction reversible, allowing self-healing and the growth of ordered layers.[14,15] Alternatively, the Schiff base reaction can be used to increase crystallinity.[16,17]

On the other hand, amorphous networks exhibit interesting properties that distinguish them from their ordered analogues. Amorphous metals without grain boundaries exhibit very high strength accompanied by low ductility.[18] Organic glasses produce smoother and pinhole-free films compared to crystalline materials.[19] Defects in graphene open a band gap in its electronic structure and populate it with in-gap states.[20] And although defects in conductors commonly lower conductivity, π-electrons can extend partially through an amorphous conjugated 2D polymer and reduce its electronic gap compared to the molecular repeat unit.[21] Currently, porous glassy metal-organic frameworks are investigated as hybrid inorganic–organic materials for CO_2 adsorption.[22]

Molecular engineering of building blocks in triphenylarene based 2D structures have shown to cause a significant change in their material properties such as photocatalytic hydrogen evolution.[23] Here, we describe two networks prepared from molecular building blocks that differ in the atomic composition of the central arene ring (Carbon-Hydrogen in **0N** replaced by Nitrogen in **3N**; Scheme 1). Under similar growth conditions, the resulting polymers have different defect densities. Molecular dynamics simulations are helpful to rationalize pore size distributions and can provide design principles that are much needed for improving the order in the polymers.

[a] Patrick Alexa, Pascal Gröger, Dr. Claudius Morchutt, Dr. Vijay Vyas, Prof. Bettina V. Lotsch, Prof. J. Christian Schön, Dr. Rico Gutzler, Prof. Klaus Kern
Max Planck Institute for Solid State Research
Heisenbergstrasse 1
70569 Stuttgart, Germany
E-mail: r.gutzler@fkf.mpg.de
[b] Prof. Christina Oligschleger
Hochschule Bonn-Rhein-Sieg
von-Liebig-Str. 20
53359 Rheinbach, Germany
[c] Dr. Claudius Morchutt, Prof. Klaus Kern
Institut de Physique
École Polytechnique Fédérale de Lausanne (EPFL)
1015 Lausanne, Switzerland
[d] Prof. Bettina V. Lotsch
Department of Chemistry
University of Munich (LMU)
Butenandtstraße 5-13
81377 München, Germany

Supporting information for this article is given via a link at the end of the document

Methods

Experiments

Experiments were carried out in ultra-high vacuum (UHV) at a pressure below 5×10^{-10} mbar. Prior to polymer synthesis, Au(111) single crystals were cleaned by repeated Ar^+-sputtering and annealing (825 K) cycles. The porous 2D polymers were synthesized through sublimation of brominated precursor molecules 1,3,5-Tris-(4-bromophenyl)-benzene (**0N**, Sigma-Aldrich) and 2,4,6-Tris-(4-bromophenyl)-1,3,5-triazine (**3N**, synthesized according to Ref.[23]) from quartz crucibles and their thermal activation in an Ullmann-like polymerization reaction on the surface. Sublimation temperatures were 475 K for **0N** and 515 K for **3N**, while the Au substrate was held at 565 K, see Scheme 1a. The STM images were recorded at room temperature and WsXM[24] was used for image analysis.

Ring statistics were gathered from large-area overview STM images. Only closed pores were counted; incomplete pores were not considered. Pores comprised of more than nine molecules were not included in the statistics.

In addition to the count of polygons, the local environment of the amorphous network was investigated. Ring neighborhoods of a vertex were counted as $\alpha\beta\gamma$-clusters, where a vertex is a point shared by three adjacent polygons α, β, and γ. Histograms of $\alpha\beta\gamma$-clusters were extracted from the same STM images from which the ring-size distribution has been taken.

Theory

Molecular dynamics (MD) on ensembles of up to 5750 molecules per periodically repeated simulation cell were performed in order to gain insight into network formation. A simplified model of the molecule was constructed that captures all relevant molecular interactions. Each molecule consists of a central unit A that is surrounded by three additional units B in a trigonal planar fashion (cf. Scheme 1b). The resulting $A(B)_3$ building units are treated as quasi-rigid molecules, i.e. interactions occur only between 'unified' subunits belonging to different building units.

The force-field that describes the intermolecular interactions consists of two- and three-body-contributions. The two-body-interaction is a Lennard-Jones term and an additionally interaction accounts for effective long-range interactions via a quasi-Coulomb-like term – again between subunits of different molecules. To include three-body interactions we apply a Stillinger-Weber potential. Details on the model of the molecule and the force field are given in the Supporting Information.

The empirical parameters of the force field are adjusted to mimic the experimentally observed rings size distributions. Since two different molecules are employed in the experiments that generate two noticeably different distributions, we have to change the potential parameters to realize the different behaviors of the experimental systems and to account for the different molecules. The potentials that yielded the best fit during a large number of test simulations for small system sizes (c.f. Supporting Information) are named potentials 1 (MD run I) and 2 (MD run II) in the following.

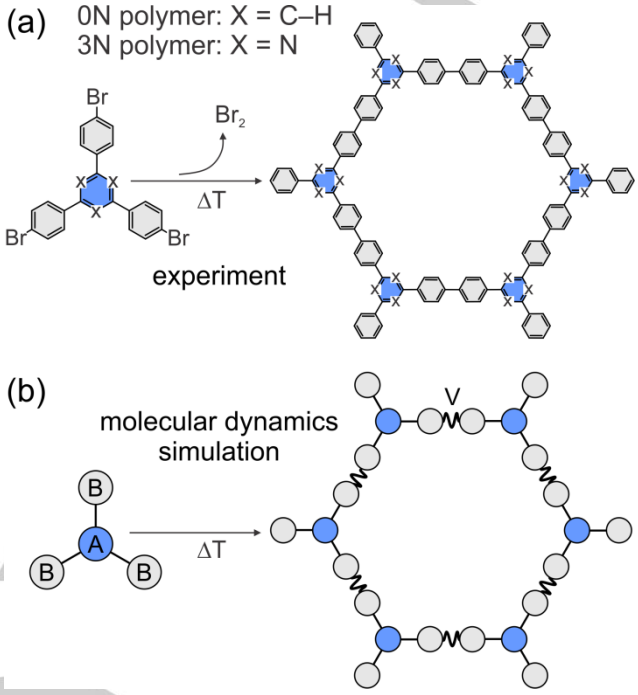

Scheme 1. (a) Ullmann-like coupling synthesis pathway. (b) Model molecule used in molecular dynamics simulation with subunits A and B and intermolecular potential V.

For the above mentioned potentials 1 (MD run I) and 2 (MD run II), we extend the system size to 5737-5750 molecules (for fifteen different starting structures). The starting structures are prepared from trigonal lattice structures from which 10% of the molecules have been removed at random and the remaining building units randomly laterally shifted by 1.00 to 1.25 Å and furthermore rotated by a random angle. The structures are heated to 2650 K during the runs. For the sake of numerical stability, the MD time step is 2 fs, and the simulations last for 120000 steps. We apply periodic boundary conditions in the MD-simulations and constant pressure is set up to establish NpT-ensembles (canonic ensembles).

Analysis of the networks

Of particular interest is the analysis of the simulated networks built up from the molecules as function of time. For this purpose, we developed a set of analysis algorithms that extract the adjacency matrix of the polymer, the ring distribution, and the distribution of $\alpha\beta\gamma$-clusters.

In particular, in addition to the simple statistics of how often rings of a certain size are observed in the experiment or the simulation, we also register the statistics of ring-triplets (or $\alpha\beta\gamma$-clusters), where three polygons of size α, β, and γ share a

common vertex. Note that such a vertex corresponds to one molecule, and each molecule can participate in up to three rings. This approach was previously used to classify short-range correlations in 2D silicon oxide.[25] Ignoring correlations, the expected occurrence of an $\alpha\beta\gamma$ -cluster based on a given (experimental or theoretical) ring-size distribution can be computed in a first mean-field like approximation through the formula

$$\mathrm{P}(\alpha,\beta,\gamma) = \mathrm{P}_\alpha \times \mathrm{P}_\beta \times \mathrm{P}_\gamma \times \mathrm{f}(\alpha,\beta,\gamma) \qquad (1),$$

where $f(\alpha,\beta,\gamma)$ is the multiplicity, which equals one if all rings are of the same size (ring index $\alpha\alpha\alpha$), equals three if only two rings have the same size (ring index $\alpha\alpha\beta$), and equals six, if all rings are of different size (ring index $\alpha\beta\gamma$). Here, P_α is the probability of an α -gon, which is taken from the relative distribution in the ring-size histograms.

Hartree-Fock calculations

On selected ring clusters, Hartree-Fock calculations were performed with the Orca 4.01 software suite.[26] The 'Corrected small basis set Hartree-Fock method for large systems' developed by Sure & Grimme[27] was used to optimize the geometry of **0N** and **3N** $\alpha\beta\gamma$-clusters with α, β, γ = 5, 6, 7. The energy of formation is calculated for each cluster defined as the total energy of the cluster minus N times the energy of the **0N**/**3N** monomer plus n times the energy of H_2, where N is the number of **0N**/**3N** units in the cluster and n is the number of bonds formed between **0N**/**3N** molecules. Bromine is substituted by hydrogen in this model calculation. The energy of formation per molecule is calculated by dividing this number by N.

Results

Experiments

A typical STM image of the investigated polymer networks is shown in Fig. 1 for **0N**. For both molecular repeat units **0N** and **3N**, similar coverages can be achieved on the Au(111) substrate through well-established Ullmann-coupling protocols.[28] The real-space imaging capabilities of STM allow resolving the disordered nature of the network and to extract the ring-size distribution. Presumably, the optimal structure from an energetic point of view is an ordered hexagonal network, but pentagons and heptagons are observed with similar frequency. The networks resemble in their amorphous structure those reported previously by several groups for **0N** under different synthesis conditions.[8,9,12] Magnifying the structures discloses the connectivity between molecular repeat units. Most molecules belong to up to three polygons but molecules that terminate without binding to other molecules can also be observed (Fig. 2). The ratio of unreacted to reacted functional groups as a measure of disorder has been explored elsewhere.[29]

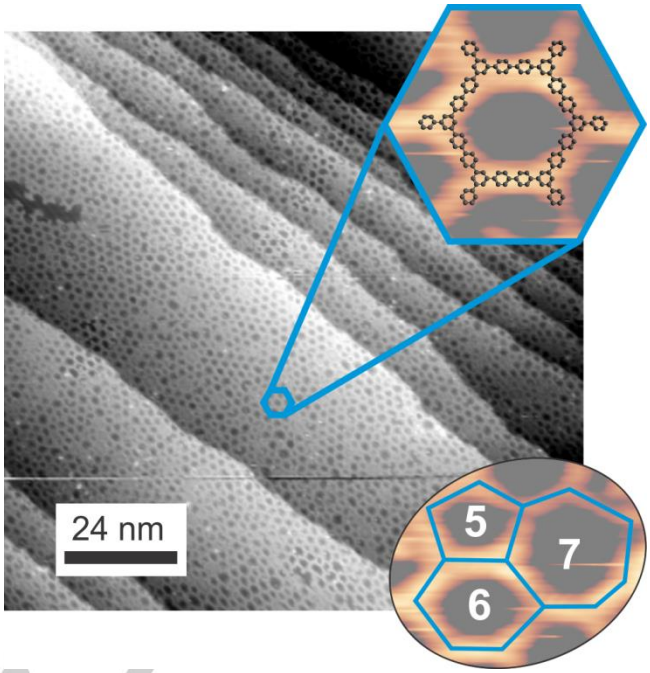

Figure 1. Typical STM topograph of the amorphous 2D polymer **0N** (U = −1.3 V, I = 0.3 pA). Insets: zoom into a hexagon with superimposed chemical structure and close-up of a cluster made from a pentagon, a hexagon, and a heptagon.

A histogram of the occurrence of α -gons (α = 4…9) is shown in Fig. 2c for **0N** and 2d for **3N**. Although the preparation methods are almost identical and differ, if anything, only in the deposition flux, the ring size histograms are markedly different. Hexagons are always found to be the dominant structural motif, but the presence of nitrogen heteroatoms in the triazine ring of **3N** lowers the relative number of pentagons compared to hexagons. A very minor occurrence of 4- and 9-membered rings is observed for **0N**, which is not observed in the **3N** statistics. Apart from the ring-size distribution, the local structure of the amorphous network can be extracted from the STM images. As mentioned above, a vertex in the network is a point shared by three adjacent polygons (cf. lower right inset in Fig. 1 for an example of a vertex shared by a pentagon, a hexagon, and a heptagon). Labelling these local environments by the size of the sharing polygons α, β, and γ the occurrence of each $\alpha\beta\gamma$-cluster can be plotted in a histogram for **0N** (Fig. 3a) and **3N** (Fig. 3b). Alongside, the expected distribution of $\alpha\beta\gamma$-clusters computed via formula (1) is plotted in gray. Marked differences between observation and model (1) are apparent. For example, the observed count of 555-clusters is much lower than the expected count, whereas 666-clusters are observed more frequently than expected.

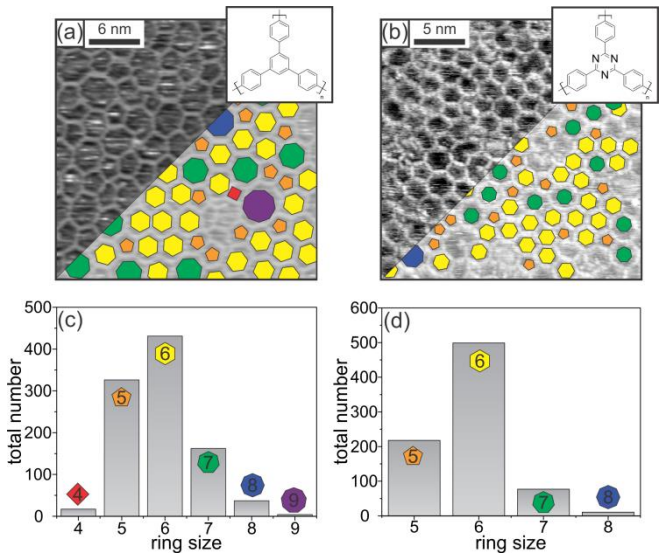

Figure 2. STM topograph of (a) **0N** (U = −1.0 V, I = 0.7 pA) and (b) **3N** (U = −1.2 V, I = 0.2 pA) with overlaid coloured polygons. (c) Ring-size distribution of **0N**. (d) Ring-size distribution of **3N**.

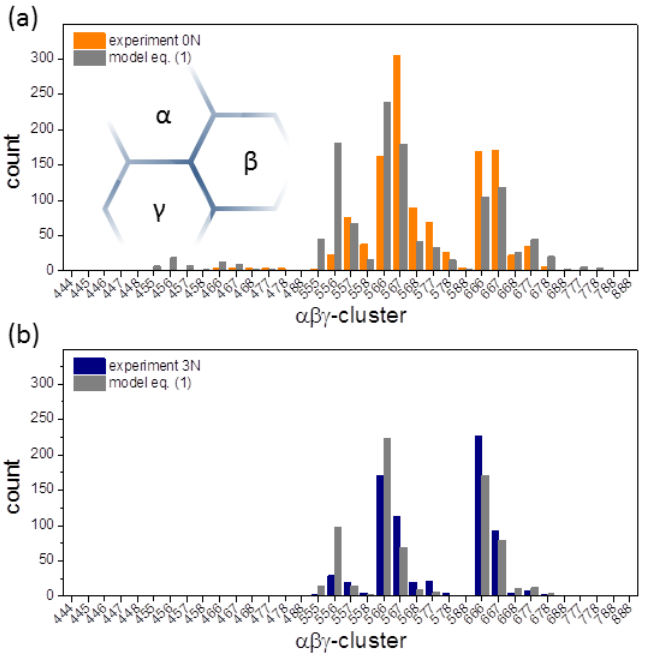

Figure 3. (a) αβγ-cluster model. (b) Expected αβγ-cluster distribution (grey) and measured distribution (orange) for **0N**. (d) Expected αβγ-cluster distribution (grey) and measured distribution (blue) for **3N**.

Theory

After an initial screening of force field parameters we chose two sets that mimic in appearance and ring size distributions the experimental data of Fig. 2. The configuration of potential 1 (MD run I) is reproduced in Fig. 4a after an MD-simulation time of 220 ps. One notices the overall homogeneity of the network, combined with a lack of any obvious crystallinity in the structure in agreement with experimental STM images. Polygons of different sizes constitute the building units of the polymer sheet. Figure 4b shows the potential energy vs. the logarithm of time, averaged over fifteen runs. After an initial settling phase of about 20 ps, the energy begins to decrease at a constant rate as function of the logarithm of time, typical for simulations of amorphous or glassy systems.[30] Clearly, we are very far from equilibrium in a state of marginal ergodicity,[31,32] where aging processes are expected to take place.[33] For comparison, we also plot the potential energy vs. log(t) when starting the system from the perfect hexagonal lattice (presumably the ground state of the system). Besides noting that the potential energy of the hexagonal lattice fluctuates about a constant value (typical for a system in equilibrium), we see that it would take four to six orders of magnitude longer simulation times than we have used until we would reach the ground state from our initial random configurations. MD run II (see Supporting Information) would take even 2 orders of magnitude longer than MD run I to reach the ground state energy.

Figure 5a,b shows the evolution of the (averaged) ring-size distribution as function of time for both MD runs. We note that the total number of rings slowly increases. The fraction of four- and eight-membered rings noticeably decreases, while both the number of five- and six-membered rings increases such that their ratio remains relatively constant. In both cases, the 6-membered rings are the most abundant species, followed by 5- and 7-membered rings. The number of energetically expensive 4- and 8-membered rings, which form in early stages of the simulation, decreases with time, while 5-, 6-, and 7-membered rings increase in abundance. The most obvious difference between the two MD runs is the relative abundance of hexagons, which is much larger in MD run II than in MD run I. Similarly to the time evolution of the ring distribution, we can plot the time evolution of the (averaged) $\alpha\beta\gamma$-cluster distribution for three points in time (t = 20 ps, t = 100 ps and t = 220 ps) for potentials 1 & 2 (Fig. 5c,d). The total number of $\alpha\beta\gamma$-clusters increases with time whereas the overall relative abundance of clusters appears to change only little between 100 and 220 ps. Alongside 666- and 667-clusters, 566-, 567- and 568-clusters are the cluster species often most observed. MD run II is marked by a larger occurrence of the aforementioned clusters with repect to the remaining $\alpha\beta\gamma$-clusters, whereas in MD run I the difference is not as prominent. We note that for all parameter values chosen, and in spite of the rather large simulation temperatures, the relative ring size distributions and the cluster distributions stabilize far from the ground state distribution, although they keep evolving in an exponentially slow fashion, of course.

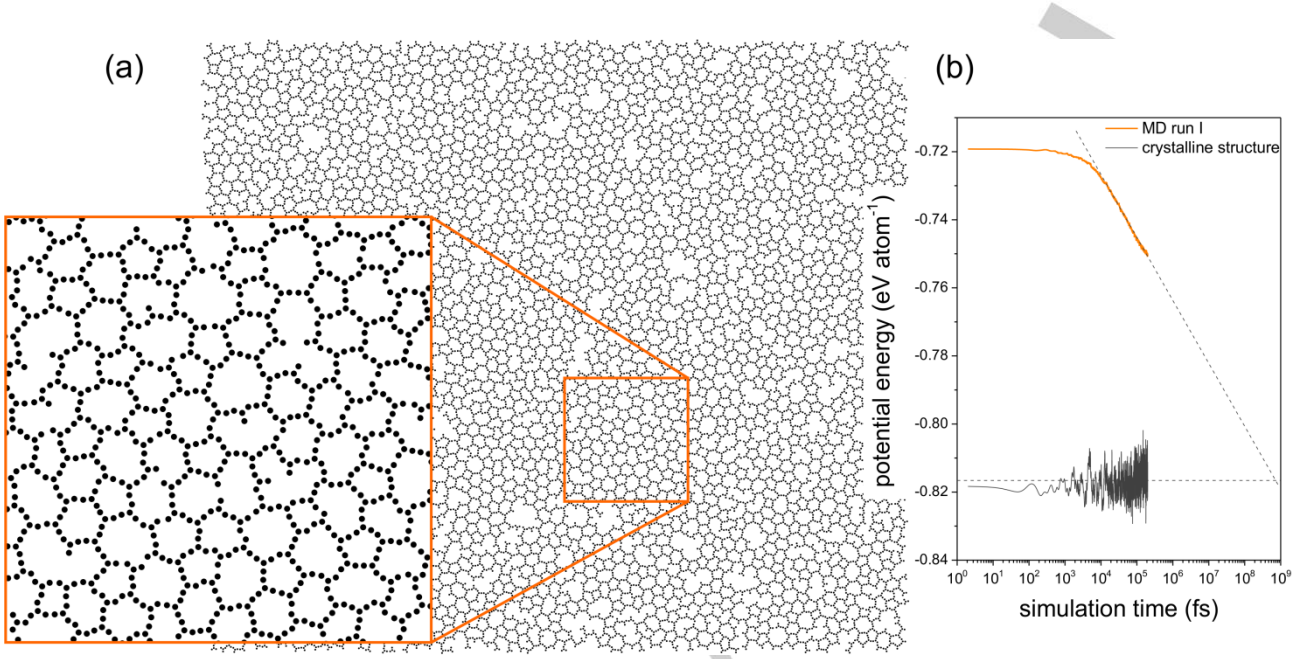

Figure 4. (a) Configuration of an amorphous network consisting of 5750 molecules in a variable periodic simulation cell, after an MD-simulation of 220 ps with potential 1 (MD run I) at 2650 K. (b) Potential energy per atom vs. log(t) (measured in MD-steps: 1MD-step = 2 fs) at 2650 K for MD run I (potential 1). Orange line: energy averaged over fifteen independent simulations; black solid line: single simulation for a perfect hexagonal lattice (ground state of the system) at 2650 K; black dotted lines: averaged energy of the crystalline state (horizontal line) and straight line "fit" of the simulations in the glassy state (after the initial settling-time) drawn to guide the eye regarding the times needed to anneal all defects and reach the crystalline ground state.

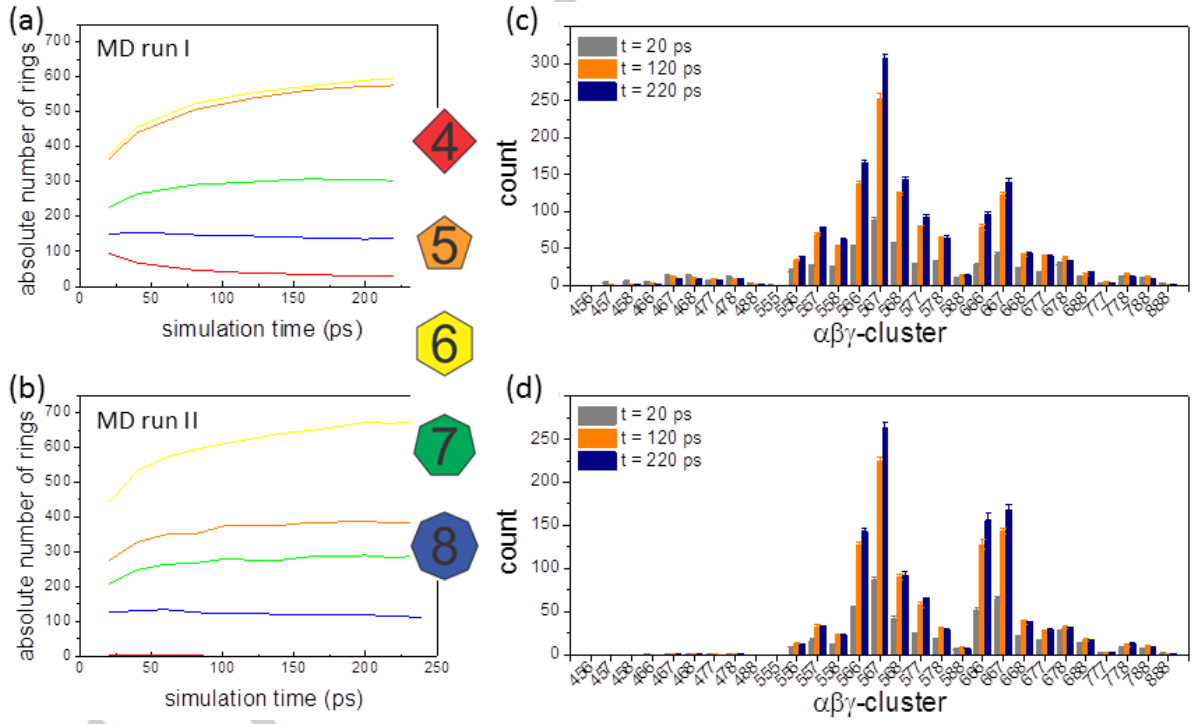

Figure 5. Rings size distributions shown as function of time (in ps). (a) Number of rings for potential 1; (b) number of rings for potential 2. (c) $\alpha\beta\gamma$-cluster distributions for potential 1 as function of time averaged over 15 configurations. Colour code: Gray: t = 20 ps; orange: t = 120 ps; blue: t = 220 ps. (d) $\alpha\beta\gamma$-cluster distributions for potential 2 as function of time averaged over 15 configurations.

Discussion

Different values of the potential produce different types of ring-size distributions. For example lower values of the intermolecular A–A–A interaction result in a relatively large abundance of 5-membered rings, whereas intermediate values of the A–A–A interaction yield a relatively larger number of 6-membered rings (c.f. Supporting Information). From these MD-simulations we can chose those two potentials that fit the experimental ring-size distributions (MD run I and MD run II), i.e. realizations of an effective potential by different kinds of molecules. Accordingly, since the **0N** ring-size statistic shows a large number of pentagons, we chose a potential with small A–A–A interaction, and a large A–A–A interaction for **6N** to account for the larger abundance of hexagons. Fig. 6a,c combines the ring-size histograms of **0N** with MD run I and Fig. 6b,d **3N** with MD run II and an overall agreement can be observed. The difference between the two MD runs is the larger A–A–A interaction by a factor of ten of MD run II compared to MD run I, and a two-fold larger B–A–B/B–B–A interaction. The second metric we employ to check whether the MD-simulation is a good fit for the experiments is a comparison of the $\alpha\beta\gamma$-cluster distributions. Experimental data from Fig. 3 of **0N** and **3N** are plotted together with the final MD distribution for comparison in Fig. 7. For **0N** and MD run I, the data agree nicely with each other. For example, 555-clusters are almost absent, 666-clusters appear with comparable frequency and both show a very large number of 567-clusters. The agreement of **3N** with MD run II is less good. In the following, we will discuss first what the origin of the agreement in **0N** might be, and then possible differences in the case of **3N**.

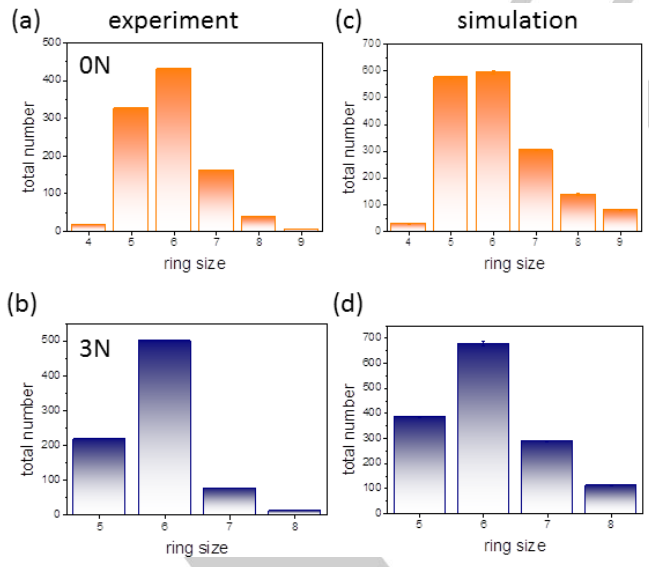

Figure 6. Histograms of ring-size distribution (a) **0N** from experiment, (b) **3N** from experiment, (c) MD run I (potential I), and (d) MD run II (potential II).

Comparing the mean-field like distribution (computed according to equation (1)) with the measured distribution (Fig. 3a for **0N**) yields only a poor agreement for **0N**. Prominent are the deviations for example in the 555, 666, and 567 clusters. More 555 clusters are expected from equation (1) than are observed, and fewer 666 clusters are expected than observed. This can be explained by the large strain that a 555 cluster would impose on the polymer structure. Forcing a 555 cluster into a planar shape requires energy to strain bonds and angles. A 666 cluster is flatter from the start and little energy is required to enforce planarity. On the other hand, a heptagon can compensate the stress built up by a pentagon in the structure, which is why 567 clusters are observed more often than expected. This argument is supported by Hartree-Fock calculations. The calculated energy of formation per molecule in **0N** is lowest in the 666-cluster and about 30% larger in the 555-cluster (40% in **3N**), i.e. more energy is required for the 555-cluster to form compared to the 666-cluster. The formation energy of the 567-cluster of **0N** lies in-between these two and is about 15% higher than the one of the 666-cluster (10% in **3N**). Responsible for the higher energy in the 555-cluster is the higher strain in the cluster. For three pentagons to connect, they have to buckle out of the plane, see Fig. 8a. Less buckling appears in the 666- and 567-clusters (Fig. 8b,c). On the surface, as observed in STM, the polymer is flat; all buckling is smoothed out by van-der-Waals interactions of the polymer with the gold substrate. Due to this flattening, the 555-cluster becomes even more energetically expensive, and thus does not appear in the observed sample. The deviation from expectation if random polygons are drawn from the distribution of Fig. 2 is a consequence of short-range correlation that appears in the polymer network. Small rings with less than 6 vertices are found in the neighborhood of large rings with more than 6 vertices. The ring distribution is clearly not random but adheres to recurrent structural motifs that are dictated by the drive to minimize strain. The correlation originates from the strain that accompanies certain $\alpha\beta\gamma$-clusters and makes them less likely than other clusters with less strain.

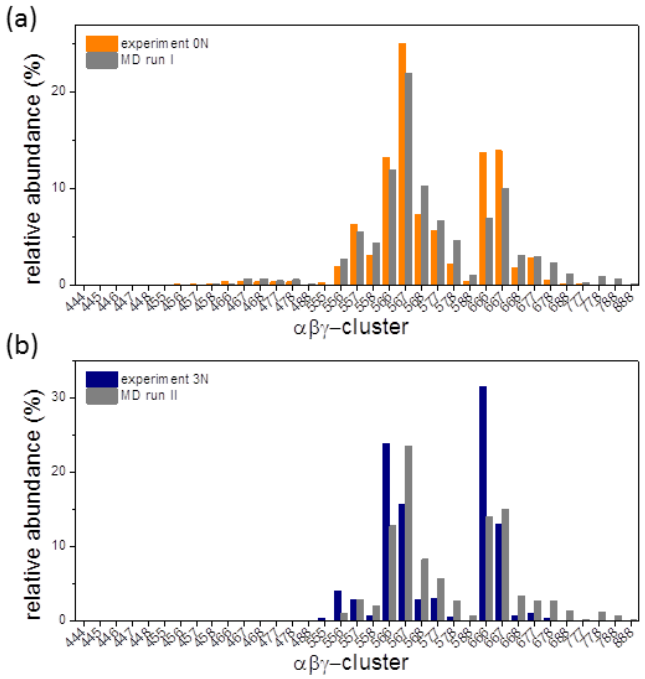

Figure 7. (a) αβγ-cluster distribution from MD-simulation (grey) and experiment (orange) for **0N** and MD run I. (b) αβγ-cluster distribution from MD simulation (grey) and experiment (blue) for **3N** and MD run II.

The agreement of both ring-size and $\alpha\beta\gamma$ -cluster distribution for **0N** and MD run I is not present in **3N** and MD run II to the same degree. Whereas the ring-size distributions compare rather well also for **3N** and MD run II, the $\alpha\beta\gamma$-cluster distribution shows marked differences. The very high frequency of occurrence of 666-clusters in the experiment leads us to believe that the experimental system is closer to the thermodynamically expected hexagonal lattice than the simulation is. This might be due to simulation times that are too short for the system to have made significant progress towards equilibrium. Figure 4b shows that the average potential energy of the MD runs steadily decreases, but on exponentially slow time scales, i.e. the time needed for the simulation to evolve towards a higher abundance of 6-membered rings increases exponentially. The relative abundance of 6-membered rings keeps increasing while the number of smaller rings remain constant or even decreases (Fig. 5b). Interestingly, the match between **3N** and the mean-field model of equation (1) is rather good compared to **0N**. The Hartree-Fock calculations show that **3N** some $\alpha\beta\gamma$-clusters require less energy to be incorporated compared to **0N**, thus the energy penalty is lower and the polygons are more likely to tessellate the surface in a random manner without the limitations imposed by energy of formation that hinders random tessellation of **0N**. Additonally, the triazine vertices of 3N impose fewer sites for steric H···H clashes between hydrogen atoms of neighboring cyclic compounds, which will lead to less energy required to enforce planarity in **3N** vs. **0N**. This in turn will make **3N** more defect tolerant and its cluster distribution closer to equation (1). The correlation on short length scales that is observed in **0N** is absent in **3N** due to the different energy required for cluster formation and for enforcing planarity. The chemical structure of the precursor molecule is thus a design criterion for tuning spatial correlations.

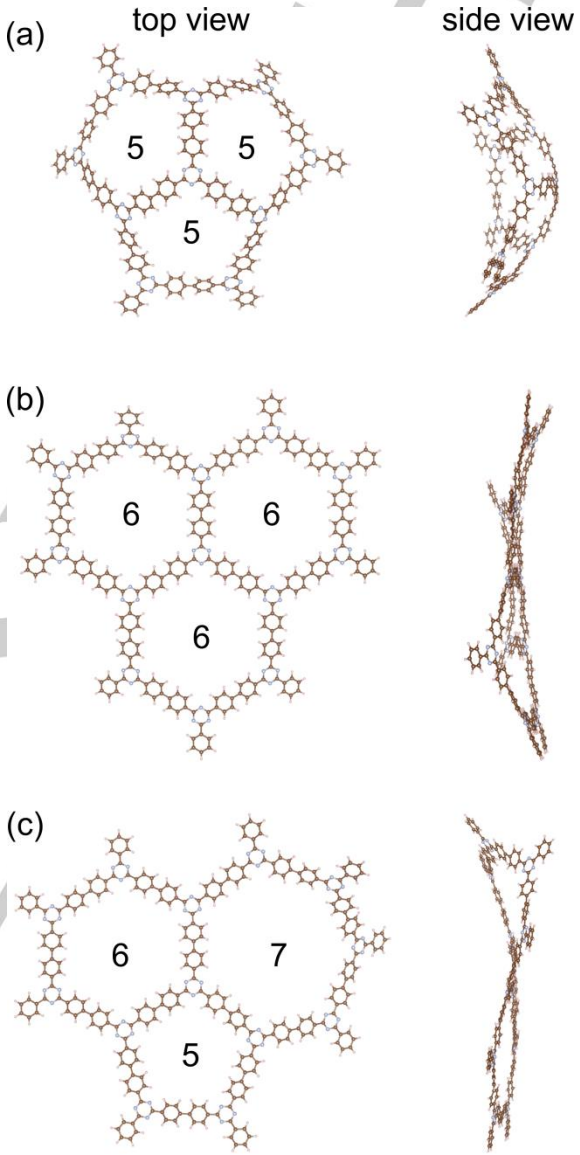

Figure 8. Top and side view of 3 different αβγ-cluster: (a) 555-cluster, (b) 666-cluster, (c) 567-cluster.

The potential energy of the calculated network structure plotted as a function of the logarithm of time (c.f. Fig. 4b above) highlights that even after rather long times the network does not settle into an energetic minimum. The energy decreases continuously with evolved simulation time, and the system evolves towards the energy of the optimal hexagonal lattice on exponentially increasing time scales, a typical aging behavior as mentioned earlier. A thermodynamic minimum is not reached, and probably will not be achieved, even after very long times.

The experimental structures can thus be expected to keep changing but on time scales likely irrelevant for experimental studies, and simulations are expected to have to run at least 4-6 orders of magnitude longer in order to reach the (presumably ground state) hexagonal lattice. This aging process is slower in potential 2 than in potential 1. Along with the continuously decreasing energy comes a restructuring of the network. The number of pores increases with time for both potentials 1 & 2 (Fig. 5a,b) as does the relative abundance of hexagonal rings. Accordingly, the $\alpha\beta\gamma$-cluster distribution keeps changing over time (Fig. 5c,d) and evolves towards a distribution consisting of those clusters with the lowest energy of formation. The aging rate depends on the choice of potential in the MD-simulation, and conversely on the choice of precursor molecule, i.e. its coupling strength and stiffness in the newly formed bonds. Unless easy breaking of the bonds is ensured – in the form of reversible bonds – perfect equilibrium will take a long time to be reached, even at elevated temperatures. On the other hand, if a particular amorphous structure is desired, for example for enhanced structural stability, then the choice of the appropriate precursor molecule can guarantee metastable structures which are aging on sufficiently slow time scales.

Conclusions

The measured ring-size distribution can be matched by a similar calculated distribution from molecular dynamics simulations. What gives additional weight to the suitability of the calculations to adequately mimic the experiments are the similarities in the relative abundance of $\alpha\beta\gamma$-clusters. This shows that not only the distributions as a property of the networks are similar, but also that short-range correlations of pore neighborhoods are identical. Accepting the validity of the calculations, we can propose design principles that would increase order in the networks. These include stiffening the A–A–A interaction and employing intermolecular interactions that allow for fast aging of the structure.

Further studies are needed for a full understanding of the growth kinetics of 2D polymers on surfaces. For one, changing the molecular repeat units to incorporate the design principles is one way, e.g. through including bulky groups at the molecules that hinder the formation of pores smaller than hexagons. On the other hand, defects in the growth template, for example step edges, should be accounted for both in experiments and in simulation. These can function as nucleation sites for growing polymer crystallites and skew the optimal growth towards small domain, high-defect density structures. Lastly, it would be interesting to study the evolution of ring and $\alpha\beta\gamma$-cluster distributions over long time scales and to investigate whether leaving the sample stored for very long times alters these distributions towards a higher abundance of 6-membered rings, and possibly generates nearly crystalline subregions.

Acknowledgements

BVL acknowledges financial support by an ERC Starting Grant (project COF Leaf, grant number 639233), the cluster of excellence e-conversion (DFG) and the Center for Nanoscience (CeNS).

Keywords: amorphous 2D polymer • molecular dynamics • ring-size statistics • scanning tunnelling microscopy • short-range correlation

[1] A. P. Côté, A. I. Benin, N. W. Ockwig, M. O'Keeffe, A. J. Matzger, O. M. Yaghi, *Science* **2005**, *310*, 1166–70.

[2] F. Haase, E. Troschke, G. Savasci, T. Banerjee, V. Duppel, S. Dörfler, M. M. J. Grundei, A. M. Burow, C. Ochsenfeld, S. Kaskel, et al., *Nat. Commun.* **2018**, *9*, 2600.

[3] D. P. Goronzy, M. Ebrahimi, F. Rosei, Arramel, Y. Fang, S. De Feyter, S. L. Tait, C. Wang, P. H. Beton, A. T. S. Wee, et al., *ACS Nano* **2018**, *12*, 7445–7481.

[4] S. Weigelt, C. Busse, C. Bombis, M. M. Knudsen, K. V. Gothelf, E. Lægsgaard, F. Besenbacher, T. R. Linderoth, *Angew. Chemie Int. Ed.* **2008**, *47*, 4406–4410.

[5] M. Marschall, J. Reichert, A. Weber-Bargioni, K. Seufert, W. Auwärter, S. Klyatskaya, G. Zoppellaro, M. Ruben, J. V Barth, *Nat. Chem.* **2010**, *2*, 131–137.

[6] S. Krotzky, C. Morchutt, V. S. Vyas, B. V. Lotsch, R. Gutzler, K. Kern, *J. Phys. Chem. C* **2016**, *120*, 4403–4409.

[7] N. A. A. Zwaneveld, R. Pawlak, M. Abel, D. Catalin, D. Gigmes, D. Bertin, L. Porte, *J. Am. Chem. Soc.* **2008**, *130*, 6678–6679.

[8] M. O. Blunt, J. C. Russell, N. R. Champness, P. H. Beton, *Chem. Commun.* **2010**, *46*, 7157–7159.

[9] R. Gutzler, H. Walch, G. Eder, S. Kloft, W. M. Heckl, M. Lackinger, *Chem. Commun.* **2009**, *29*, 4456–4458.

[10] T. Faury, S. Clair, M. Abel, F. Dumur, D. Gigmes, L. Porte, *J. Phys. Chem. C* **2012**, *116*, 4819–4823.

[11] M. Bieri, M.-T. Nguyen, O. Gröning, J. Cai, M. Treier, K. Aït-Mansour, P. Ruffieux, C. A. Pignedoli, D. Passerone, M. Kastler, et al., *J. Am. Chem. Soc.* **2010**, *132*, 16669–16676.

[12] J. Eichhorn, D. Nieckarz, O. Ochs, D. Samanta, M. Schmittel, P. J. Szabelski, M. Lackinger, *ACS Nano* **2014**, *8*, 7880–7889.

[13] W. Rżysko, D. Nieckarz, P. Szabelski, *Adsorption* **2019**, *25*, 75–85.

[14] C.-Z. Guan, D. Wang, L.-J. Wan, *Chem. Commun.* **2012**, *48*, 2943.

[15] J. F. Dienstmaier, A. M. Gigler, A. J. Goetz, P. Knochel, T. Bein, A. Lyapin, S. Reichlmaier, W. M. Heckl, M. Lackinger, *ACS Nano* **2011**, *5*, 9737–9745.

[16] X.-H. Liu, C.-Z. Guan, S.-Y. Ding, W. Wang, H.-J. Yan, D. Wang, L.-J. Wan, *J. Am. Chem. Soc.* **2013**, *135*, 10470–10474.

[17] Y. Yu, J. Lin, Y. Wang, Q. Zeng, S. Lei, *Chem. Commun.* **2016**, *52*, 6609–6612.

[18] M. Chen, *NPG Asia Mater.* **2011**, *3*, 82–90.

[19] M. D. Ediger, J. de Pablo, L. Yu, *Acc. Chem. Res.* **2019**, *52*, 407–414.

[20] P. Kot, J. Parnell, S. Habibian, C. Straßer, P. M. Ostrovsky, C. R. Ast, **2018**, arXiv:1811.00087.

[21] L. Cardenas, R. Gutzler, J. Lipton-Duffin, C. Fu, J. L. Brusso, L. E. Dinca, M. Vondráček, Y. Fagot-Revurat, D. Malterre, F. Rosei, et al.,

Chem. Sci. **2013**, *4*, 3263.

[22] C. Zhou, L. Longley, A. Krajnc, G. J. Smales, A. Qiao, I. Erucar, C. M. Doherty, A. W. Thornton, A. J. Hill, C. W. Ashling, et al., *Nat. Commun.* **2018**, *9*, 5042.

[23] V. S. Vyas, F. Haase, L. Stegbauer, G. Savasci, F. Podjaski, C. Ochsenfeld, B. V. Lotsch, *Nat. Commun.* **2015**, *6*, 8508.

[24] I. Horcas, R. Fernández, J. M. Gómez-Rodríguez, J. Colchero, J. Gómez-Herrero, A. M. Baro, *Rev. Sci. Instrum.* **2007**, *78*, 013705.

[25] C. Büchner, L. Liu, S. Stuckenholz, K. M. Burson, L. Lichtenstein, M. Heyde, H.-J. Gao, H.-J. Freund, *J. Non. Cryst. Solids* **2016**, *435*, 40–47.

[26] F. Neese, *Wiley Interdiscip. Rev. Comput. Mol. Sci.* **2012**, *2*, 73–78.

[27] R. Sure, S. Grimme, *J. Comput. Chem.* **2013**, *34*, 1672–1685.

[28] Q. Fan, J. M. Gottfried, J. Zhu, *Acc. Chem. Res.* **2015**, *48*, 2484–2494.

[29] O. Ourdjini, R. Pawlak, M. Abel, S. Clair, L. Chen, N. Bergeon, M. Sassi, V. Oison, J.-M. Debierre, R. Coratger, et al., *Phys. Rev. B* **2011**, *84*, 125421.

[30] A. Hannemann, J. C. Schön, M. Jansen, P. Sibani, *J. Phys. Chem. B* **2005**, *109*, 11770.

[31] S. Neelamraju, C. Oligschleger, J. C. Schön, *J. Chem. Phys.* **2017**, *147*, 152713.

[32] J. C. Schön, M. Jansen, *Int. J. Mater. Res.* **2009**, *100*, 135–152.

[33] L. G. E. Struik, *Physical Aging in Amorphous Polymers and Other Materials*, Elsevier Sci. Publ. Comp., Amsterdam-Oxford-New York, **1978**.

Entry for the Table of Contents (Please choose one layout)

Layout 1:

ARTICLE

Text for Table of Contents

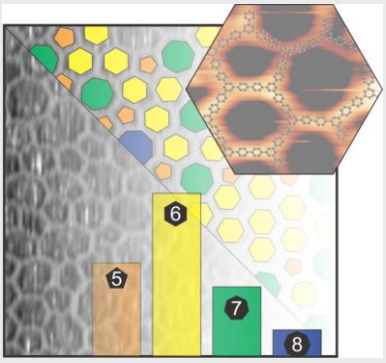

*Author(s), Corresponding Author(s)**

Page No. – Page No.

Title